Supramolecular chemistry enables vat photopolymerization 3D printing of novel water-soluble tablets

Jun Jie Ong [a], Yee Lam Chow [a], Simon Gaisford [a], Michael T. Cook [a], Thomas Swift [b], Richard Telford [b], Stephen Rimmer [b], Yujia Qin [c], Yang Mai [c], Alvaro Goyanes [a,d,e], Abdul W. Basit [a,d,*]

[a] *Department of Pharmaceutics, UCL School of Pharmacy, University College London, 29-39 Brunswick Square, London WC1N 1AX, UK*
[b] *School of Chemistry and Biosciences, University of Bradford, Richmond Road, BD7 1DP, UK*
[c] *School of Pharmaceutical Sciences (Shenzhen), Sun Yat-sen University, Guangzhou 510275, China*
[d] *FabRx Ltd., 3 Romney Road, Ashford, Kent TN24 0RW, UK*
[e] *Departamento de Farmacología, Farmacia y Tecnología Farmacéutica, I+D Farma (GI-1645), Facultad de Farmacia, Instituto de Materiales (iMATUS) and Health Research Institute of Santiago de Compostela (IDIS), Universidade de Santiago de Compostela, 15782, Spain*

ARTICLE INFO

ABSTRACT

Vat photopolymerization has garnered interest from pharmaceutical researchers for the fabrication of personalised medicines, especially for drugs that require high precision dosing or are heat labile. However, the 3D printed structures created thus far have been insoluble, limiting printable dosage forms to sustained-release systems or drug-eluting medical devices which do not require dissolution of the printed matrix. Resins that produce water-soluble structures will enable more versatile drug release profiles and expand potential applications. To achieve this, instead of employing cross-linking chemistry to fabricate matrices, supramolecular chemistry may be used to impart dynamic interaction between polymer chains. In this study, water-soluble drug-loaded printlets (3D printed tablets) are fabricated via digital light processing (DLP) 3DP for the first time. Six formulations with varying ratios of an electrolyte acrylate monomer, [2-(acryloyloxy)ethyl]trimethylammonium chloride (TMAEA), and a co-monomer, 1-vinyl-2-pyrrolidone (NVP), were prepared to produce paracetamol-loaded printlets. ^{1}H NMR spectroscopy analysis confirmed the integration of TMAEA and NVP in the polymer, and residual TMAEA monomers were found to be present only in trace amounts (0.71 – 1.37 %w/w). The apparent molecular mass of the photopolymerised polymer was found to exceed 300,000 Da with hydrodynamic radii of 15 – 20 nm, estimated based on ^{1}H DOSY NMR measurements The loaded paracetamol was completely released from the printlets between 45 minutes to 5 hours. *In vivo* single-dose acute toxicity studies in rats suggest that the printlets did not cause any tissue damage. The findings reported in this study represent a significant step towards the adoption of vat photopolymerization-based 3DP to produce personalised medicines.

1. Introduction

3D printing (3DP), or additive manufacturing, has been actively investigated as one of the enabling technologies for the impending era of personalized medicines (Deon et al., 2022; Elbadawi et al., 2021; Jørgensen et al., 2023; Medicines & Healthcare products Regulatory Agency, 2021; Seoane-Viaño et al., 2023). This paradigm shift, away from the traditional one-size-fits-all approach towards patient care, promises enhanced clinical outcomes by maximizing efficacy while minimizing adverse side effects. Enthusiasm in the field has led to

numerous 3DP drug-loaded pharmaceutical products, such as polypills (Pereira et al., 2020; Robles-Martinez et al., 2019; Xu et al., 2020), drug-loaded intravaginal rings (Januszewicz et al., 2020; Tiboni et al., 2021; Utomo et al., 2023), hearing aids (Vivero-Lopez et al., 2021), patches for topical delivery (Bagde et al., 2023; de Oliveira et al., 2021; de Oliveira et al., 2023), and cardiovascular prosthesis and implants (Adhami et al., 2023; Martin et al., 2021). There are numerous types of 3DP technologies, which all share the general working principle of building a 3D geometry layer-by-layer based on a computer-aided design (CAD). According to the American Society for Testing and Materials (ASTM), 3DP

technologies can be broadly classified into seven categories, based on the feedstock and method of layer manufacturing: vat photopolymerization, material jetting, binder jetting, material extrusion, powder bed fusion, sheet lamination, and directed energy deposition (American Society for Testing and Material, 2021). Each technology has their own unique strengths and weaknesses, which in turn guide their potential applications.

Amongst 3DP technologies, vat photopolymerization affords the highest resolution, enabling the fabrication of complex micrometer-scale models (Xu et al., 2021a). In vat photopolymerization, 3D objects are produced by irradiating a vat of liquid photopolymer resin with light, inducing a polymerization reaction that solidifies the irradiated resin (Li et al., 2020; Ng et al., 2020; Xu et al., 2021a). Vat photopolymerisation comprises several light-based printing technologies, of which digital light processing (DLP), liquid crystal display (LCD), and stereolithography (SLA) are the most widely available. Unlike other 3DP technologies such as material extrusion and powder bed fusion, the feedstock used in vat photopolymerization are not subjected to high temperatures, therefore making the technology better suited for heat-labile drugs (Xu et al., 2021a). In the medical field, DLP and SLA have already been employed in the dental industry for medical modelling, restorative dentistry, digital orthodontics, and dental implants (Dawood et al., 2015; Rouzé l'Alzit et al., 2022).

In the pharmaceutical industry, vat photopolymerization 3DP is being extensively investigated for the fabrication of personalised medicines and medical devices, such as printlets (Robles-Martinez et al., 2019; Xu et al., 2020), patient-specific implants (van Lith et al., 2016; Vivero-Lopez et al., 2021; Xu et al., 2021b), and microneedles (Detamornrat et al., 2022; Economidou et al., 2019; Lim et al., 2021). Interest in the use of DLP and SLA for personalised medicines, despite efforts elsewhere in the use of other 3DP technologies for the same purpose, stems from its high dimensional accuracy that assures accurate and precise dosing and enables the fabrication of intricate structures for unique and tunable drug release profiles. Apart from research on the application of vat photopolymerization 3DP, advances in the technology have also been made to improve its suitability for pharmaceutical manufacturing. Recently, the LCD screen of mobile devices, such as smartphones and tablets, was used as the light source for small-scale LCD 3D printers (Xu et al., 2021c). The portability of these mobile systems allows them to be easily deployed in remote regions, providing people living in typically hard-to-reach regions access to their medications on-demand. On the other hand, a novel vat photopolymerization 3D printing technology known as *volumetric printing* has recently emerged, promising superior printing speeds and structural isotropy (de Beer Martin et al., 2019; Kelly et al., 2019; Loterie et al., 2020; Rodríguez-Pombo et al., 2023). In volumetric printing, the entire 3D geometry is fabricated simultaneously rather than in a layer-by-layer fashion, drastically shortening the time needed to print an object. This state-of-the-art technology has been investigated for pharmaceutical purposes, wherein torus-shaped printlets were produced within seconds (Rodríguez-Pombo et al., 2022). As described, enthusiasm towards vat photopolymerization 3DP among pharmaceutical researchers continues to grow due to the superior printing accuracy it affords, despite some of its limitations that have hampered clinical translation.

One of the drawbacks of vat photopolymerization 3DP is the lack of resins that produce water-soluble 3D-printed structures. This has typically been due to the use of cross-linkers (e.g., di- or tri-acrylates) in resin formulations that result in dense, permanent, and insoluble cross-linked networks. Specifically in the pharmaceutical space, polyethylene glycol diacrylate (PEGDA) is heavily used, such as for producing hydrogel microneedles (Gittard et al., 2010; Han et al., 2020; Yao et al., 2020), drug-loaded implants and scaffolds (Ranganathan et al., 2020; Vehse et al., 2014; Yang et al., 2020), and personalised tablets (Robles-Martinez et al., 2019; Rodríguez-Pombo et al., 2023; Xu et al., 2020; Xu et al., 2021c). Uncovering a solution to this limitation will broaden the application of vat photopolymerization 3DP. Drug release will no longer

be limited to sustained release profiles, widening the armamentarium that may be feasibly produced with vat photopolymerization. Oral drug delivery is the most common form of medicines administration, accounting for 60% of commercially available small-molecule drugs, due to its convenience and generally non-aversive nature that leads to high patient compliance (Alqahtani et al., 2021). Therefore, the development of water-soluble vat photopolymerized structures is important for the clinical translation of vat photopolymerization-based 3DP for personalised medicines.

Wilts et al have successfully printed water-soluble structures with vat photopolymerization 3D printing using a combination of an electrolyte acrylate, [2-(acryloyloxy)ethyl]trimethylammonium chloride, and 1-vinyl-2-pyrrolidone (NVP) (Wilts et al., 2019). The polymers in the 3D-printed parts were held together by supramolecular interactions as opposed to covalent bonds in a cross-linked network. The study aimed to apply these resins to produce soluble support scaffolds and did not investigate its potential pharmaceutical applications. The presence of a drug molecule in the 3D-printed structure could interfere with the supramolecular interactions between polymers, thereby affecting printability and dissolution rates. Similarly, the addition of non-reactive diluents might accelerate dissolution rates that could be beneficial for the fabrication of immediate-release dosage forms.

Therefore, this study aims to develop drug-loaded photopolymerizable resin formulations that, upon photopolymerization via DLP 3DP, will be dissolvable in water. The printability, physicochemical properties, and dissolution profiles of six different formulations were investigated. *In vivo* single-dose acute toxicity studies were also conducted using three formulations to investigate their biocompatibility. The work presented herein represents a significant step towards the clinical applicability of vat photopolymerization for personalized medicines.

2. Materials & methods

2.1. Materials

Paracetamol, [2-(acryloyloxy)ethyl]trimethylammonium chloride solution (TMAEA) (80 wt% in water), 1-vinyl-2-pyrrolidinone (NVP), and lithium phenyl-2,4,6-trimethylbenzoylphosphinate (LAP, MW 294.21 g/mol, ≥ 95%) were purchase from Sigma-Aldrich (Dorset, UK). Red food colorant (*Kroma Kolors*, Kopykake, Torrance, CA, USA) was purchased from Shesto Limited (Watford, UK). Deuterium oxide (D, 99.9%) was purchased from Cambridge Isotope Laboratories (Massachusetts, USA). All materials were used as received.

2.2. Preparation of photosensitive resins

Drug-loaded photosensitive resins were prepared in 8 mL amber vials. 0.5 % w/w of LAP was first weighed and added into the vial, followed by 0.5 % w/w of food colourant, and subsequently 5 % w/w of paracetamol. Varying ratios of TMAEA:NVP or TMAEA:NVP:Water were then added to the mixture using a Pasteur pipette (Table 1). 7 g of resin was prepared in each iteration. The final solution was thoroughly mixed at room temperature (~25 °C) until all components were completely dissolved and homogenized (up to 12 h).

2.3. 3D printing process

All printlets were printed with a commercial DLP 3D printer (*Titan2 HR*, Kudo3D Inc., Dublin, CA, USA) equipped with an HD DLP projector with a visible light source (400-700 nm). A cylinder, 10 mm diameter x 3.6 mm height, was selected as the desired 3D geometry. The 3D object was created with 123D Design (Autodesk Inc., USA) and exported as a stereolithographic file (.stl) into the Kudo3D Print Job software for slicing into 0.025 mm thick layers. The printer XY resolution was set to 23 μm. The exposure time for formulations without water was 30 s per

Table 1
Composition of formulations and respective exposure times used for printing.

Formulation	LAP (% w/w)	TMAEA (% w/w)	NVP (% w/w)	Water (% w/w)	Food colorant (% w/w)	Paracetamol (% w/w)	Exposure time per layer (s)
TN100	0.50	94.00	-	-	0.50	5.00	30
TN90	0.50	84.60	9.40	-	0.50	5.00	30
TN80	0.50	75.20	18.20	-	0.50	5.00	30
TNW100	0.50	61.10	-	32.90	0.50	5.00	120
TNW90	0.50	54.99	6.11	32.90	0.50	5.00	120
TNW80	0.50	48.88	12.22	32.90	0.50	5.00	120

layer, and 120 s per layer for those containing water (Table 1). The lift speed was set at 15 mm/min and the lift height was set at 2 mm. After printing, printlets were rinsed for 1 min in isopropyl alcohol (IPA), and then post-cured in a Form Cure (Formlabs Inc., Somerville, MA, USA) at room temperature (~25 °C) for 30 min.

2.4. Physicochemical characterisation of printlets

2.4.1. Differential Scanning Calorimetry (DSC)

DSC measurements were performed with a Q2000 DSC (TA instruments, Waters, LLC, New Castle, DE, USA) to characterise paracetamol powder and printlets. Samples were heated from 0 to 195 °C at 10 °C/min, then cooled to 0 °C at 10 °C/min, and finally heated to 195 °C at a heating rate of 10 °C/min. Nitrogen was used as a purge gas with a flow rate of 50.0 mL/min for all experiments. Data were collected with TA Advantage software for Q series (version 2.8.394, TA instruments, Waters LLC, New Castle, DE, USA) and analysed using TA Instruments Universal Analysis 2000. TA aluminium pans and pin-holed hermetic lids (Tzero) were used with an average sample size of 3.0–5.0 mg.

2.4.2. Thermogravimetric analysis (TGA)

Thermogravimetric analysis (TGA) was performed with a Discovery TGA (TA Instruments, Waters, LLC, USA). Samples were heated from 30 to 195 °C at 10 °C/min in open aluminium pans, and nitrogen was used as a purge gas with a flow rate of 25 mL/min. Data collection and analysis were performed and calculated using TA Instruments Trios software.

2.4.3. X-ray powder diffraction (XRPD)

Discs (23.0 mm diameter x 1.0 mm height) were 3D-printed using each formulation for XRPD analysis with the same printing settings as those used to prepare the respective printlets. Powdered samples of pure paracetamol were also analysed by XRPD. XRPD patterns were obtained with a Rigaku MiniFlex 600 (Rigaku, Wilmington, MA, USA) equipped with a Cu X199 ray source (λ = 1.5418 Å). The intensity and voltage applied were 15 mA and 40 kV. Samples were scanned between 2θ = 3–60° with a stepwise size of 0.02° at a speed of 5°/min.

2.4.4. Fourier-Transform infrared spectroscopy (FTIR)

The infrared spectra of formulations before and after DLP 3D printing were collected using a Spectrum 100 FTIR spectrometer (PerkinElmer, Waltham, MA, USA). All samples were scanned over a range of 4000–650 cm^{-1} at a resolution of 4 cm^{-1} for 6 scans. The spectra of pure paracetamol drug powder, water, TMAEA, and NVP were collected as references.

2.4.5. Nuclear Magnetic Resonance (NMR) spectroscopy

All NMR spectra were recorded in 99.9% D2O. 1H-NMR spectra of NVP, TMAEA, LAP, paracetamol, food colourant, and printlet samples were obtained separately. 9–10 mg of sample was dissolved in 1 mL of D2O for analysis. 1H NMR spectra of the samples were obtained using a Bruker AVANCE 400 MHz spectrometer. Data acquisition and processing were performed using standard TopSpin Software (Bruker, UK). Additional diffusion measurement studies were conducted on a Bruker AV NEO 600 MHz spectrometer equipped with a dedicated diffusion (Bruker diffBB) probe to determine analyte diffusion and viscosity of sample solutions. For viscous polymer samples, liquids were dissolved at 1 mg/mL concentrations, with the diffusion experiment set up using γ 26752 rad / (s*Gauss), δ 0.0036 s, Δ 0.0599 s. Diffusion decays of signal strength were recorded over 64 gradient steps and analysed using Topspin (v4.1.1) and the Dynamics Centre (Bruker, UK). Polymer hydrodynamic radii (R$_H$) were extracted from diffusion values (D) employing a modified Stokes-Einstein relationship (Equation (1)) where the in-solution viscosity (η) was determined using variations in solvent diffusion (Swift et al., 2017).

$$R_H = k_B T / 6\pi\eta D \tag{1}$$

Once hydrodynamic radii were determined, diffusion distributions were converted to apparent molar mass distributions by comparing hydrodynamic radii with narrow polyethylene glycol (PEG) standards of known diffusion and radii (Swift et al., 2017). After distribution smoothing was applied to overcome background noise in the data, this produced indicative molar mass averages for the bulk of the dissolved polymer (more fully described in the electronic supporting information).

2.5. Determination of drug content

2.5.1. In printlets

Printlets were dissolved in 250 mL of distilled water in volumetric flasks and placed under magnetic stirring for 24 hours (*n = 3*). The resulting solutions were diluted 5x with distilled water, and subsequently filtered through a 0.45 μm filter (Merck Millipore Ltd., Ireland) into HPLC vials. The concentration of drug in each printlet was then determined using HPLC, as later described in Section 2.7.

2.5.2. In photosensitive resins

Approximately 0.05 g of each photosensitive resin was extracted from the surface immediately after all components have been dissolved, after being left standing for 12 h, and after 24 h. These extracts were dissolved in 100 mL of distilled water in a volumetric flask and placed under magnetic stirring for 24 hours. Samples were subsequently withdrawn from the volumetric flasks and filtered through a 0.45 μm filter (Merck Millipore Ltd., Ireland) before HPLC analysis (Section 2.7) All measurements were made in triplicates.

2.6. In vitro dissolution study

Dissolution profiles for each type of Printlets were obtained using USP-II apparatus (Model PTWS, Pharmatest, Germany) (*n = 3*). The paddle speed of the USP-II was fixed at 50 rpm and the dissolution medium was maintained at 37 ± 0.5 °C. For the first 2 hours, samples were dissolved in 750 mL of 0.1 M HCl. After 2 hours, 250 mL of 0.2 M trisodium phosphate solution was added to each dissolution vessel and the pH was adjusted to 6.8 using 5.0 M NaOH solution. 2 mL samples were withdrawn at pre-defined time intervals (5, 10, 20, 30, 45, 60, 90, 120, 180, 240, 300, 360, 420, and 490 min). Samples were then filtered through a 0.45 μm filter (Merck Millipore Ltd., Ireland) and analysed using HPLC (Section 2.7).

2.7. High Performance Liquid Chromatography (HPLC)

Hewlett Packard 1260 Series HPLC system equipped with an online degasser, quaternary pump, column heater, autosampler and UV/Vis detector, was used. 20 µL of the samples were injected into an Eclipse plus C18 5 µm column, 4.6 × 150 mm (Zorbax, Agilent technologies, Cheshire, UK). Solution compounds were separated by a mobile phase consisting of 15% of methanol and 85% of water with a 1 mL/min flow rate. The process was carried on with a temperature of 40°C and eluents were then screened with a 247 nm light source.

2.8. In vivo single-dose acute toxicity study

Healthy male Sprague Dawley rats (20–25 weeks old, 350–400 g in weight) were obtained from Sipeifu Biotechnology Co. Ltd (Beijing, China). All animal procedures were performed in accordance with Ruiye Model Animal Biotechnology (Guangzhou, China) protocols (RYEth-20230405207). Animals were kept in Ruiye Model Animal Biotechnology Co. Ltd (Guangzhou, China).

Size 9h capsular printlets were printed as described in Section 2.3, using TN100, TN90 and TN80 formulations. All size 9h printlets were placed in size 9 gelatin capsules to prevent adhesion to the oesophageal walls during administration. The rats were housed at room temperature (25 °C) in a light-dark cycle of 12 h. The rats were kept in individual cages with a platform and fasted for 12 h before capsule administration until 4 h post-administration. At the start of the study, the capsules were introduced directly into the stomach of the rats using a Torpac dosing device for rodents ($n = 6$ per formulation). The body weight and food consumption of rats were recorded every day during the experiments. After 14 days, the rats were sacrificed by CO_2 asphyxiation. Heart, liver, spleen, kidney, stomach, intestine, and colon tissues were harvested for histological examination. Samples were fixed in 4.0 % para-formaldehyde and embedded in paraffin. 7–10 µm sections were stained with haematoxylin and eosin (H&E) and observed under an Olympus BX61 microscope with a SPOT Flex 64 MP digital colour camera.

2.9. Statistical analysis

Data were reported throughout as mean ± standard deviation (n = 3, unless otherwise stated). Unless otherwise stated, one way ANOVA analysis with post-hoc Tukey test at 95% significance level ($p < 0.05$) was used to analyse statistically significant difference between sample groups.

3. Results & discussion

To achieve water-soluble matrices, supramolecular interactions, such as hydrogen bonds and ion-dipole interactions, were employed to form reversible bonding between polymers. [2-(acryloyloxy)ethyl]trimethylammonium chloride (TMAEA) was included as the charged electrolyte monomer that enables strong supramolecular interactions to be formed. NVP was included in some formulations as a co-monomer to provide higher structural strength, as NVP has been found to reduce molecular oxygen-induced inhibition during photopolymerization, thereby resulting in higher acrylate bond conversions and stronger matrices (Wilts et al., 2019). Following photoradical generation, the acrylate group in TMAEA and the vinyl group in NVP undergo homolytic bond fission and radical chain-growth polymerization (Fig. 1). LAP was selected as the photoinitator due to its absorption activity in the visible light region. Red food colourant was used as a photoabsorber to attenuate non-specific photocuring, water was used as the non-reactive diluent, and paracetamol was selected as the model drug.

In this study, printlets comprising a positively charged mono-acrylate (TMAEA) and 1-vinyl-2-pyrrolidinone as photocurable monomers were successfully printed with DLP 3DP (Fig. 2A & 2B). Formulations that did not contain water (TN100, TN90, and TN80) were printable with an exposure time of 30 s per layer, whereas those with water (TNW100, TNW90, and TNW80) required 120 s exposure time per layer to be printable (Table 1). The longer exposure time required for formulations containing water is due to the relatively lower proportion of photoreactive monomers available to participate in the free radical polymerization reaction, thereby reducing the rate of photo-polymerization. The printlets that did not contain water were homogenously red in colour, while those that contained water only had a slight tint of red. The difference in colour could be attributed to dilution of the red food dye by water.

All formulations, except TN80, were printable with consistent dimensions (measured immediately after printing): printlet height ranged

Fig. 1. Schematic outlining the radical chain-growth reaction that occurs between NVP and TMAEA
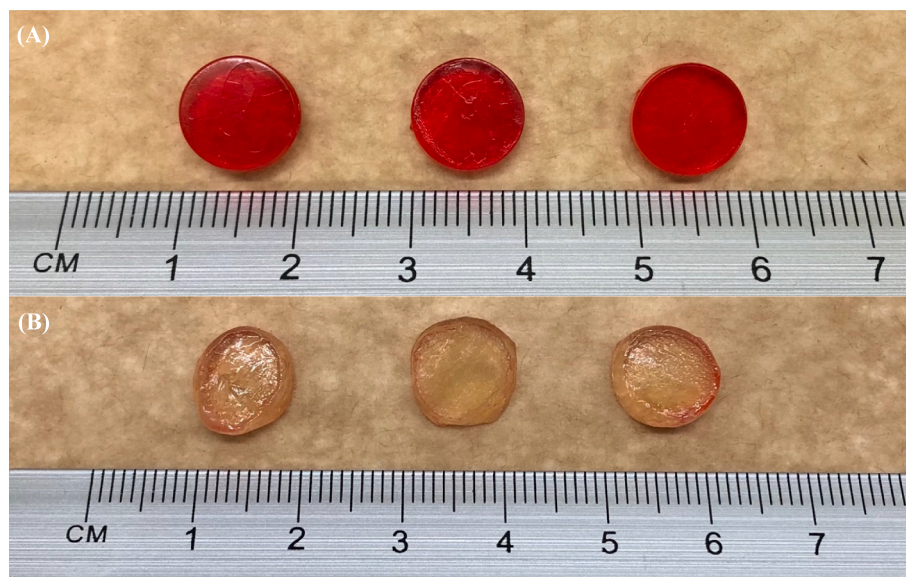
Fig. 2. Photograph of printlets (A) without water – TN100, TN90, TN80 (from left to right), and (B) with water – TNW100, TNW90, TNW80 (from left to right).

no more than ± 4.97% RSD, while printlet diameter ranged no more than ± 1.53% RSD (Table 2). The relatively wide range of height, and hence weight, for TN80 printlets is an artefact of layers being inadvertently scraped off during removal of the printlets from the build plate. This is in turn due to the highly adhesive nature of the printlets that makes removal from the build plate challenging. Conversely, high consistency in physical dimensions for TN100 and TN90 printlets translated to consistency in printlet weight. However, consistent printlet weight was not observed with all printlets containing water (TNW100, TNW90, and TNW80) despite their dimensions appearing consistent. This is likely due to TNW100, TNW90, and TNW80 printlets being notably softer and more malleable than their water-absent counterparts, which made accurately measuring their dimensions challenging.

The observed lack of structural integrity can be explained through the supramolecular interactions holding the polymer matrix together. Within each layer, polymers are held together by ion-dipole interactions between the positively charged tertiary ammonium nitrogen in TMAEA units and carbonyl C=O dipole in NVP units (Fig. 3A). Water molecules can form hydrogen bonds with the carbonyl C=O in NVP units and ion-dipole interactions with the tertiary ammonium nitrogen in TMAEA units, disrupting inter- and intra-polymer non-covalent interactions. Therefore, during printing, the polymer chains are constantly disrupted by water molecules present in the formulation, reducing the degree of

inter-polymer supramolecular interactions and thereby the density of the printed matrix. This results in a soft and malleable polymer matrix that is unable to resist even minimal external pressure, which could in turn have made measurements artificially consistent despite best efforts made to blindly take them. Therefore, while printlets containing water appear to be consistent in dimensions, their weights and qualitative observations on their weak tensile strength suggest otherwise and that layers were in fact scraped off as with TN80 printlets.

In the same vein, printlets containing water were noticeably wider and flatter after storage for 24 h in a plastic seal bag (Fig. 3B). For instance, the height of TNW100 printlets decreased by 19.1 ± 0.602% and the diameter of TNW100 printlets increased by 10.3 ± 0.106% after 24 h storage ($n = 3$). This is likely because the soft printlets were flattened by the weight of the walls of the plastic Ziplock bags that they were stored in. The poor structural integrity also explains the irregular and oval shape of TNW100, TNW90, and TNW80 printlets as pictured in Fig. 1 and Fig. 3B.

Loading of paracetamol in printlets were found to be slightly lower than the theoretical drug loading (5% w/w). No significant difference was found between the drug loading in printlets and the resins that they were derived from for TN100, TN90 and TN80, suggesting that the lower drug loading in these printlets relative to the theoretical drug load were insignificant (Fig. 4). However, post-hoc comparison of TNW100, TNW90, and TNW80 printlet and resin drug loading found significant difference between the printlet and resin drug loading (Fig. 4). Given that the formulations comprised numerous liquid components (TMAEA, NVP, and for some, water) of varying densities and paracetamol solubility, it was hypothesized that phase separation could have occurred during the preparation of the resins and prior to printing, which in turn resulted in heterogenous distribution of paracetamol. To investigate this, samples of each formulation were extracted close to the surface of the solution immediately after mixing, after standing for 12 h, and after standing for 24 h. No statistically significant difference was found between the paracetamol loading in resins for all formulations across the three time points ($p < 0.05$) (Fig. 4). This indicates that paracetamol was homogenously distributed, and phase separation did not occur in the resin formulations prior to printing.

FTIR spectroscopy was used to probe possible chemical interactions between paracetamol and the photoreactive components in the formulation, which could in turn account for the lower paracetamol loading (Fig. 5). FTIR was also used to confirm that radical polymerization between TMAEA and NVP had occurred. The spectrum obtained from
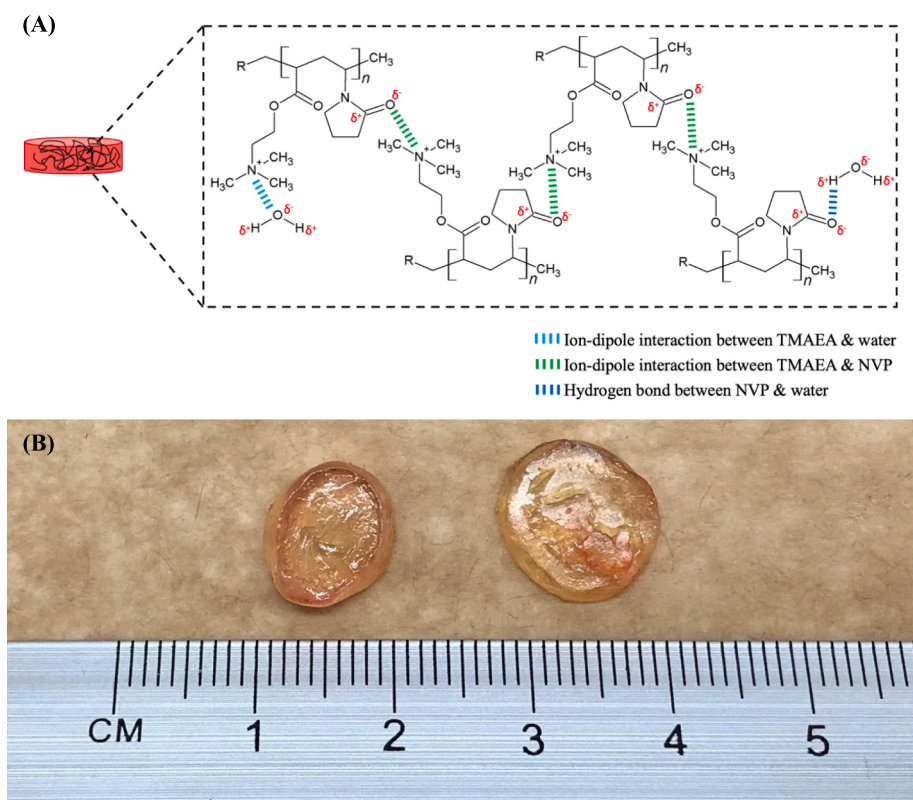
Table 2
Physical dimensions and weight immediately after printing, resin drug loading, and printlet drug loading of TN100, TN90, TN80, TNW100, TNW90, and TNW80 printlets.

Formulation	Diameter (mm) (n = 8)	Height (mm) (n = 8)	Weight (mg) (n = 8)	Resin loading (%) (n = 3)	Printlet loading (%) (n = 3)
TN100	9.88 ± 0.13	3.46 ± 0.09	302.24 ± 14.16	4.94 ± 0.05	4.89 ± 0.07
TN90	9.88 ± 0.07	3.22 ± 0.16	296.03 ± 3.59	4.98 ± 0.01	4.90 ± 0.05
TN80	9.94 ± 0.07	3.08 ± 0.42	285.25 ± 37.76	4.94 ± 0.03	4.76 ± 0.03
TNW100	9.82 ± 0.15	3.53 ± 0.04	320.59 ± 33.12	4.96 ± 0.03	4.35 ± 0.22
TNW90	9.84 ± 0.12	3.40 ± 0.11	280.26 ± 36.44	4.94 ± 0.03	4.58 ± 0.13
TNW80	9.89 ± 0.14	3.42 ± 0.08	267.75 ± 8.39	4.95 ± 0.05	4.58 ± 0.19

Fig. 3. (A) Illustration of supramolecular interactions occurring within the printlet structure. These interactions include ion-dipole interactions between TMAEA units and water molecules, ion-dipole interactions between TMAEA & NVP units, and hydrogen bonds between NVP & water. (B) Photograph of TNW100 immediately after post-curing (left) and after storage for 24 hours (right).
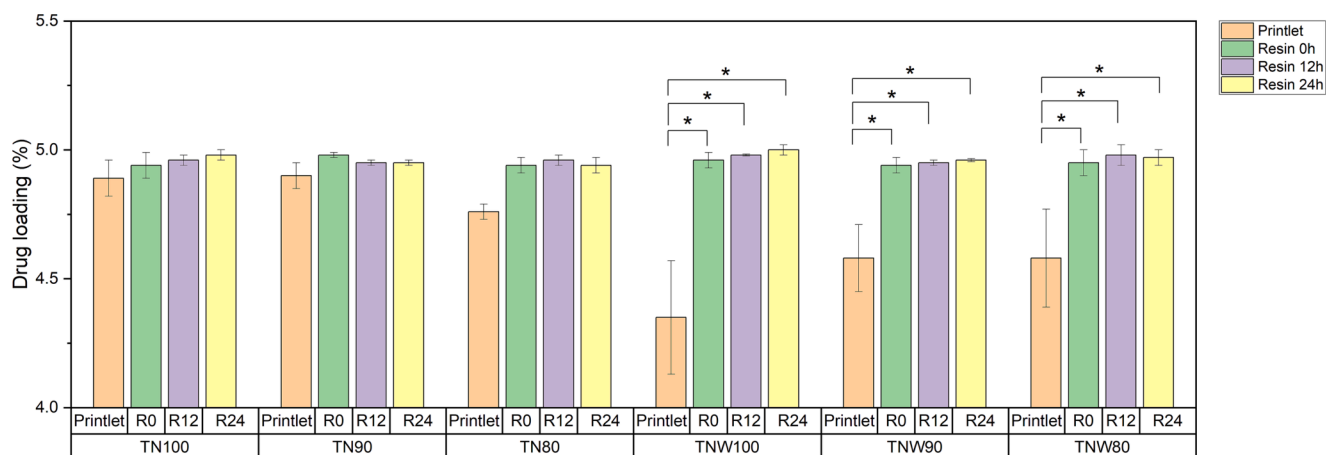

Fig. 4. Paracetamol loading in printlets, and resins prior to printing immediately after preparation (R0), after standing for 12 hours (R12), and after standing for 24 hours (R24).

paracetamol powder showed characteristic vibrational peaks at 3323 cm^{-1} (O-H stretch), 1653 cm^{-1} (secondary amide C=O stretch), 1561 cm^{-1} (secondary amide N-H bend), and 1505 cm^{-1} (C-H bend) (Trivedi et al., 2015). These vibrational peaks are visible in the absorption spectra of TN80 and TNW80 printlets and resins, except for the peak at 3323 cm^{-1} that was masked by stronger signals from TMAEA. This suggests the absence of any detectable chemical reactions, such as Michael addition, between paracetamol and the photopolymers. Photopolymerization was confirmed by analysing the absorption bands assigned to the acrylate groups in TMAEA, namely 1722 cm^{-1} (ester C=O stretch) and 1633 cm^{-1} (alkene C=C stretch). Attenuation of the

peak at 1633 cm^{-1} in the printlet FTIR spectrum compared to the resin FTIR spectrum is indicative of acrylate radical polymerization, as C=C bonds are broken and converted to C-C bonds during the reaction. In support of this, there is an increase in intensity of the vibrational peaks assigned to alkane C-H stretch (2920 cm^{-1} and 2850 cm^{-1}) in the absorption spectra of the printlets, indicating an increase in abundance of alkane groups.

Phase separation prior to printing nor chemical interactions with photoreactive components in the resin could not account for the slightly lower paracetamol loading in TNW100, TNW90, and TNW80 printlets. It is possible that phase separation occurred during the
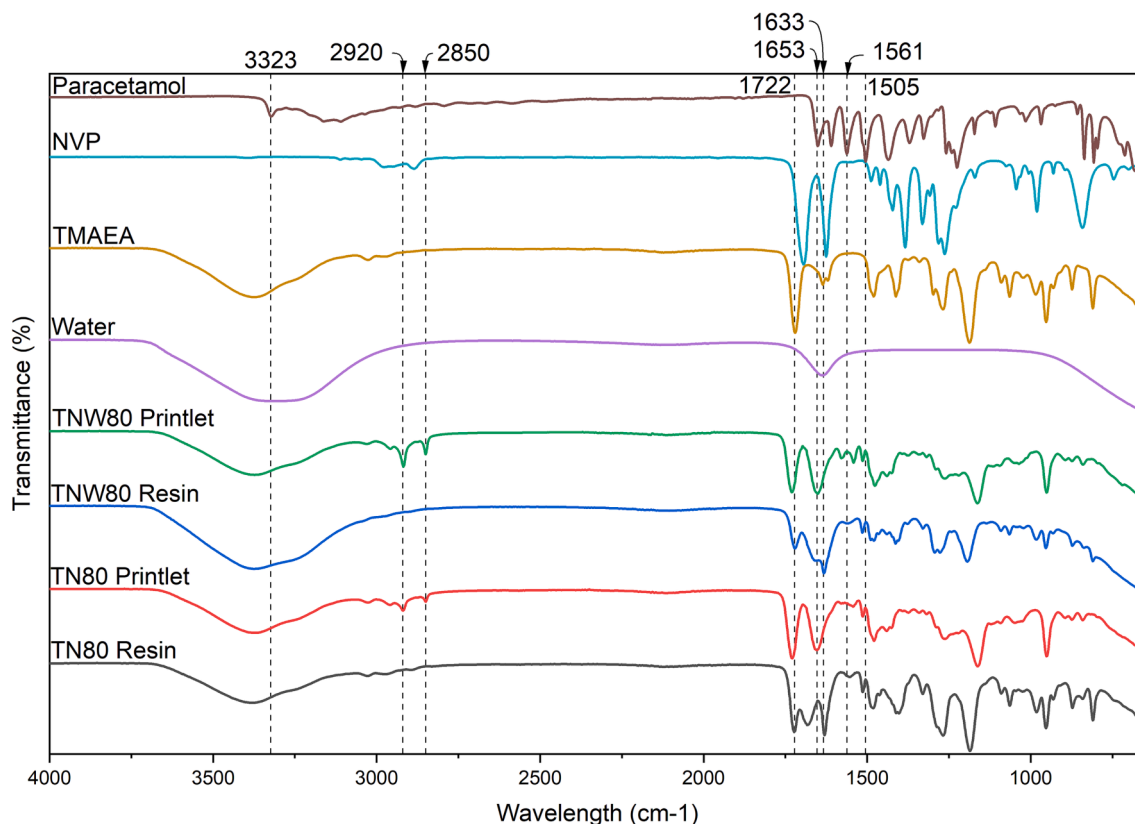
Fig. 5. FTIR spectra of paracetamol, NVP, TMAEA, water, and TNW80 and TN80 resin and printlets.

photopolymerization process. As reported by Bhavana et al., the thermodynamics of mixing changes during photopolymerization, whereby the mixing of non-polymerizing component (i.e., paracetamol) within the resin becomes thermodynamically unfavourable due to alterations to solubility parameters (Deore et al., 2021; Paquet et al., 2022). The non-polymerizing component (paracetamol) consequently diffuses away from the locus of polymerization and towards regions where it is more soluble. The extent of diffusion is dependent on the viscosity, crosslinking density, and gelation rate of the growing polymer network (Deore et al., 2021). Fast rate of gelation, high viscosity, and high crosslinking density impedes the migration of non-polymerizing molecules due to a tight polymer network. In our case, as alluded to previously, the presence of water in TNW100, TNW90, and TNW80 results in less dense polymer networks that facilitates the diffusion of non-polymerizing molecules. Water also decreases the viscosity of the resin, further enhancing the diffusion of paracetamol away from the locus of polymerization. These may therefore explain the significant difference found between resin and printlet paracetamol load for TNW100, TNW90, and TNW80. Future work could investigate the principal factor influencing the flux of non-polymerizing components, which could in turn reveal strategies to prevent reduction in drug loading. For instance, viscosity enhancers such as methylcellulose and alginic acid could be added to impede diffusion, although there likely needs to be a balance since the kinetics of radical photopolymerization is also dependent on the viscosity of the system. Nonetheless, the printlets derived from TN100, TN90, TN80, and TNW90 meets the requirements for the USP content uniformity test, with acceptance values of 4.06, 2.90, 4.84, and 13.14, respectively.

DSC and XRD analysis of the printlets and pure paracetamol powder was performed to investigate the physical state of paracetamol in the printlets. DSC analysis of pure paracetamol power revealed a melting endotherm at 169 °C (Fig. 6A). This peak was absent in the printlets' DSC thermogram, suggesting that paracetamol was completely dissolved

in the resin mixture and remained molecularly dispersed in the solid printlets. This is supported by XRD analysis, wherein the acquired X-ray diffractograms of all printlets revealed the absence of crystalline peaks corresponding to paracetamol, indicating that paracetamol was not present in its crystalline state but molecularly dispersed in the printlets (Fig. 6B). Interestingly, a broad endotherm stretching from 50 to 150 °C was observed in the DSC thermograms of all printlets. This was hypothesised to correspond to the evolution of water, and subsequently confirmed by the mass & moisture loss observed in TGA analysis (Fig. 6C) as well as the absence of this broad endotherm in the second DSC heat cycle (Fig. 6D). This was unexpected given the absence of water in TN100, TN90, and TN80 printlets, and that the extent of mass loss is similar in all printlets (13.1–15.3%). It is therefore proposed that unlike previous work where water was incorporated as a non-reactive diluent, water molecules were not retained in printlets derived from formulations containing water. Instead, the water evolving from the printlets during DSC analysis is proposed to be derived from sorbed atmospheric water, given the hygroscopic nature of the polyelectrolyte polymer.

DSC analysis also revealed that the inclusion of water in formulations influenced the polymerization reaction apart from rate deceleration. The DSC thermograms of TNW80 and TNW90 printlets showed an endotherm at 145 °C and 130 °C, respectively. This is hypothesised to correspond to the melting of PVP, given that PVP has been found to melt at 130–150 °C depending on its molecular weight. The TGA thermogram of TNW80 and TNW90 printlets also show slightly accelerated mass loss at approximately 130 °C. Therefore, the presence of water might have hindered polymerization between TMAEA and NVP monomers and thereby increase NVP polymerization to form PVP. The difference in temperature at which the PVP melting endotherm occurs in TNW80 and TNW90 printlets can be attributed to differences in the molecular weight of PVP in these printlets.

NMR spectroscopy was performed to investigate the presence of
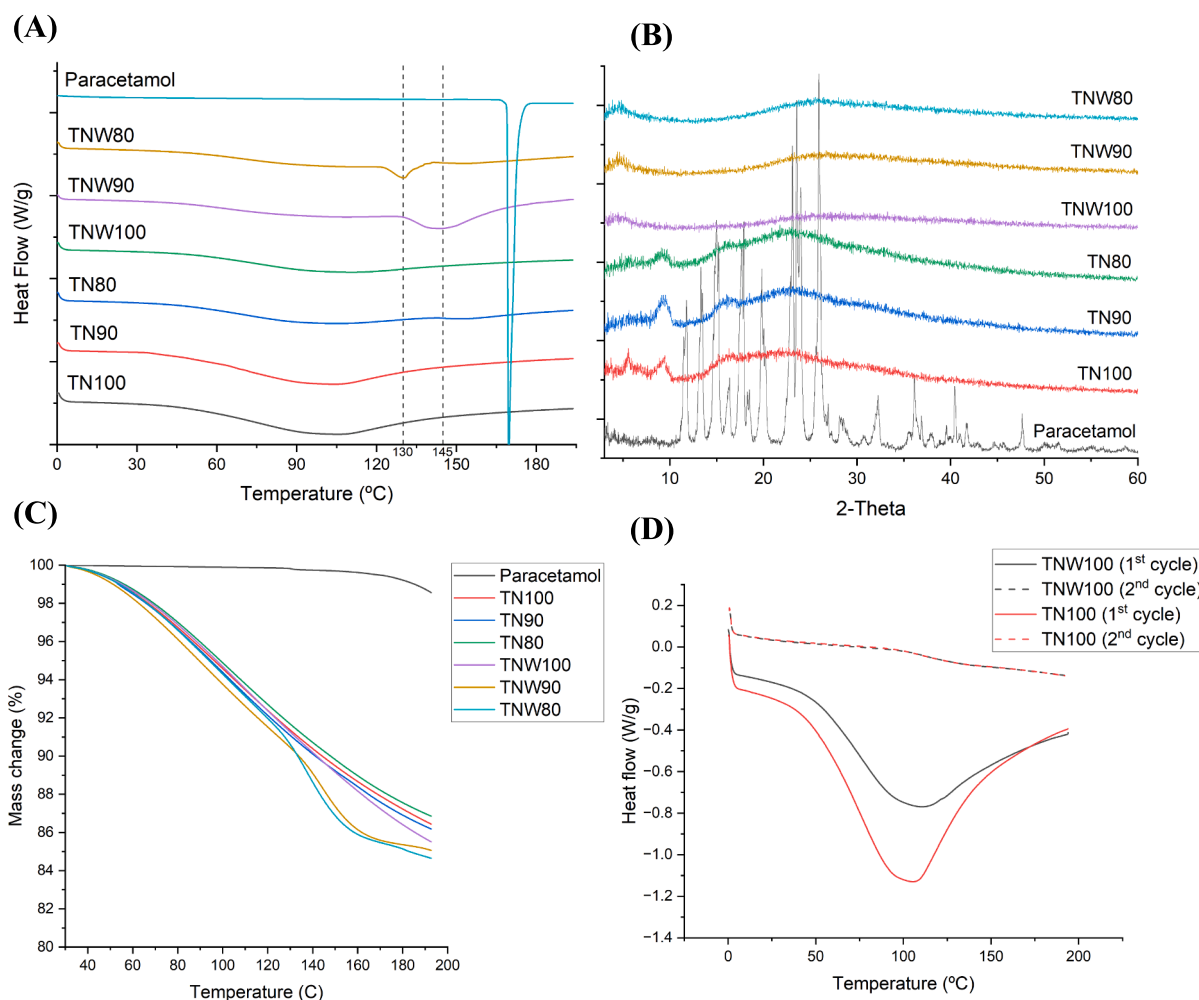
Fig. 6. (A) DSC thermogram of first heat cycle of pure paracetamol and TN100, TN90, TN80, TNW100, TNW90, and TNW80 printlets. (B) X-ray powder diffractograms of pure paracetamol and TN100, TN90, TN80, TNW100, TNW90, and TNW80 printlets. (C) TGA thermogram of pure paracetamol and TN100, TN90, TN80, TNW100, TNW90, and TNW80 printlets. (D) Representative DSC thermograms of both heating cycles of TN100 and TNW100 printlets.

unreacted TMAEA and NVP monomers after printing (Fig. 7A). The assignment of 1H signals for NVP, TMAEA, LAP, and paracetamol are provided in Fig. 7B. The signals at 6.0–6.5 ppm on the spectra of TMAEA (signal H-16, H-17, and H-18) corresponds to the CH=CH2 acrylate protons, which are absent in the spectra of TN100, TN90, and TN80. Likewise, the signal occurring at 6.9 ppm on the spectra of NVP (signal H-4) that corresponds to a CHN vinyl proton is absent in the spectra of the printed samples. Signals arising in the 6.8–7.2 region of the spectra of TN80, TN90, and TN100 arise instead from the aromatic moiety of paracetamol. As a result of the photopolymerization reaction, the acrylate C=C double bond and vinyl C=C double bond undergoes homolytic bond fission to propagate monomer and form the saturated C-C polymer backbone. Consequently, the acrylate protons and vinyl protons in TMAEA and NVP respectively are expected be in a more shielded environment post-polymerization and their signals should shift upfield. Therefore, the absence of these signals indicates that the photopolymerization reaction had occurred to completion, and any unreacted TMAEA and NVP monomers should be absent or present in only trace amounts. Estimations of the amount of unreacted TMAEA in the printlets were made by comparing the integral of the peaks corresponding to signal H-2 of paracetamol and signal H-16 of TMAEA, and using a conservative estimate that paracetamol loading was 5% in these samples. There were approximately 1.25 ± 0.25 w/w, $1.09 \pm 0.29\%$ w/w, $1.37 \pm 0.38\%$ w/w, $0.95 \pm 0.07\%$ w/w, $0.88 \pm 0.11\%$ w/w, and $0.71 \pm 0.12\%$ w/w of TMAEA remaining in TN100, TN90, TN80, TNW100,

TNW90, and TNW80 samples, respectively ($n = 3$). Taking the average weight of the printlets (Table 2), this would in turn correspond to approximately 3.78 ± 0.76 mg, 3.23 ± 0.86 mg, 3.91 ± 1.08 mg, 3.05 ± 0.22 mg, 2.47 ± 0.31 mg, and 1.90 ± 0.32 mg of TMAEA in TN100, TN90, TN80, TNW100, TNW90, and TNW80 printlets, respectively. This falls significantly below the LD50 of TMAEA as stipulated in its safety data sheet (category 4 acute oral toxicity, $LD_{50} \geq 2000$ mg/kg bodyweight). Signals arising from the alkene protons of NVP were not visible on the NMR spectra of all printlet samples.

Additionally, the signal at 3.2 ppm in the spectra of TMAEA (signal H-21) that corresponds to the methyl groups bonded to the positively charged nitrogen persisted in the spectra of TN100, TN90, and TN80, indicating that TMAEA monomers were successfully integrated into the polymer chain. Likewise, the signal at 3.7 ppm in the printlets' spectra likely corresponds to the -CH2 protons adjacent to the nitrogen atom in NVP (signal H-7 in the spectra of NVP), suggesting that NVP monomers were also successfully integrated into the polymer chain. Downshifting and broadening of this signal (from 3.6 to 3.7 ppm) is consistent with the different chemical environment observed in the polymerised sample. Signals from the phenyl protons and methyl protons of paracetamol, occurring at 6.8–7.2 ppm and 2.1 ppm respectively (signal H-1, H-2, and H-3), are still visible in the spectra of TN100, TN90 and TN80. This confirms the successful integration of paracetamol into the polymer matrix with no evidence of any undesired chemical reactions occurring between paracetamol and the reactive components of the formulation (i.
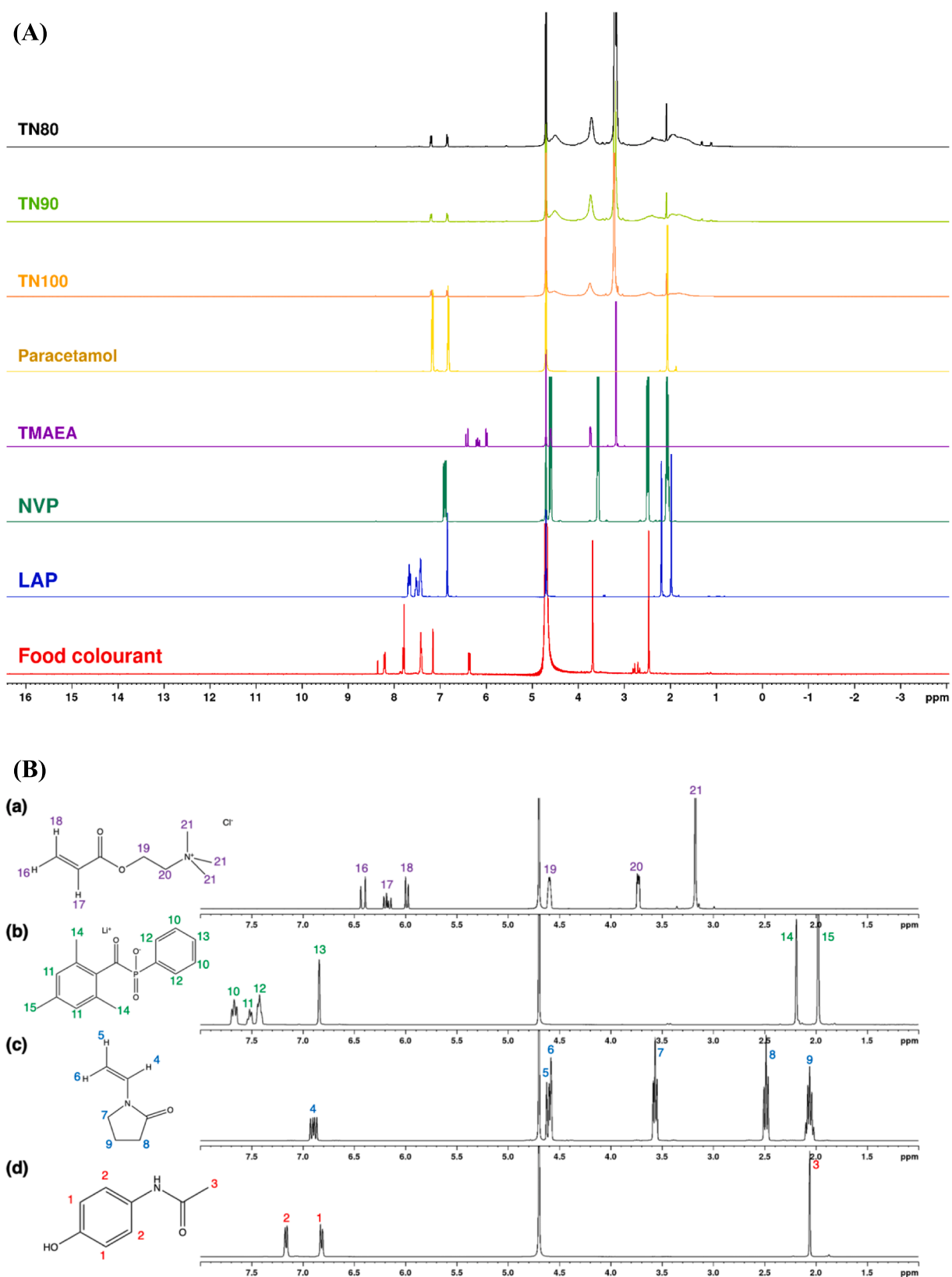
(A)

(B)

Fig. 7. (A) ^{1}H NMR spectra (D$_2$O) of NVP, TMAEA, LAP, paracetamol, food colourant, and TN100, TN90, and TN80 samples. (B) ^{1}H NMR spectra (D$_2$O) of (a) TMAEA, (b) LAP, (c) NVP, and (d) paracetamol.

e., TMAEA, NVP, and LAP). Broad peaks occurring at 1.0–4.6 ppm are also observed in the spectra of TN100, TN90 and TN80. These are characteristic of protons in repeated subunits of the polymer chain, as protons in the chain are in slightly different chemical environments due to intra- and inter-chain supramolecular interactions.

^{1}H DOSY NMR measurements were performed to interrogate the diffusion characteristics of both the polymer and the incorporated paracetamol after dissolution for samples TN100, TN90, and TN80. These provided supporting information that the paracetamol diffuses considerably more quickly than the polymer (diffusion coefficients of *ca.* 5.0 x 10^{-10} m^2/s and *ca.* 1 x 10^{-11} m^2/s, respectively), and that its change in diffusion in the presence of the polymer can be associated only with the change of sample viscosity. Thus, the data suggests that the two entities are separate, i.e. there is no evidence of association of the paracetamol to the polymer post-dissolution. Furthermore, ^{1}H DOSY NMR measurements were used to calculate chain hydrodynamic radii of the dissolved polymers in solution and thus compare samples TN100, TN90, and TN80 directly with one another. It is noteworthy that attempts at characterising these properties through gel permeation chromatography (GPC), as is conventional, proved unsuccessful due to the high molecular weight of the samples.

The raw diffusion coefficients have been used to predict hydrodynamic radii in solution using the Stokes-Einstein relationship (see Section 2.4.5) with viscosity correction from the solvent diffusion (Swift et al., 2017). This leads us to propose that sample TN100, TN90 and TN80 have hydrodynamic radii of 20, 19 and 15 nm respectively. Comparison of these values with references of known molecular weight (narrow distribution polyethylene glycol, PEG) determined in previous studies suggest that the polymers are very large, with molar masses exceeding 300,000 Da (fully detailed in the Supplementary material 1). Fig. 8 presents a representative ^{1}H DOSY NMR spectrum sample (TN80), showing the diffusion characteristics of the polymer and paracetamol in solution (prepared at 1 mg/mL in D2O) and apparent size distributions.

In-vitro drug release studies revealed that paracetamol release commenced immediately during the gastric phase (pH 1.2) and were not affected by the change of pH of the dissolution media (to pH 6.8) (Fig. 9). Apart from TN100, printlets derived from the remaining 5 formulations released the bulk of their paracetamol load within the gastric phase (2 hours), while it took TN100 printlets ~5 h to reach 100% drug release. Printlets derived from all formulations were also completely solubilised during the dissolution process. However, except for TNW90 printlets, the remaining formulations failed to meet the FDA's acceptance criteria for immediate-release solid oral dosage form

drug products, i.e., 80% of the drug load should be released in 30 minutes. Additionally, while TNW90 printlets met this criterion, the high standard deviation obtained warrants further replicates to ascertain its performance. Large standard deviations were observed for all printlets containing water (TNW100, TNW90, and TNW80), which could be attributed to the malleable and highly adhesive nature of the printlets that led to variable surface-area-to-volume (SA/V) ratio. Since the SA/V ratio is a key parameter to dissolution rate, as described by the Noyes-Whitney equation, varying SA/V ratios resulted in variable rates of drug release.

To facilitate the clinical applicability of this resin formulation, the biocompatibility of these formulations must be investigated. Therefore, *in vivo* single-dose acute toxicity studies were performed to investigate the potential toxicity of the printlets. To minimise harm done to the animals, the theoretical toxicity of the components of the printlets were considered. The cytocompatibility of LAP has been demonstrated through its frequent use in 3D bioprinting formulations, while the food colourant used as the photoabsorber has already been certified safe for consumption. The primary components of concern are TMAEA and NVP. While NVP is a toxic substance as a monomer, it polymerizes to form polyvinylpyrrolidone (PVP), a polymer that is in the FDA's Inactive Ingredient Database and has been extensively used in the pharmaceutical industry. ^{1}H NMR spectroscopy data also indicated that any unreacted NVP monomers was not detectable. On the other hand, the safety data sheet for TMAEA provided by Sigma-Aldrich indicate that it can cause GHS Category 4 acute oral toxicity (LD$_{50}$ $\geq$ 2000 mg/kg bodyweight), suggesting that the amount of residual TMAEA monomers in the printlets (as estimated through ^{1}H NMR spectroscopy) should be safe. Risks associated with the potential toxicity of TMAEA-co-NVP polymer are mitigated by its large apparent size, as observed through ^{1}H DOSY NMR measurements, which should prevent the partitioning of TMAEA-co-NVP polymers into cells. Since cationic lipids mainly exert their cytotoxicity through intracellular mechanisms, namely caspase activation dependent signalling pathway and mitochondrial dysfunction (Cui et al., 2018), there is reason to believe that TMAEA-co-NVP would not be cytotoxic.

In vivo toxicity studies were therefore conducted using male Sprague Dawley rats. Formulations containing water (TNW100, TNW90, and TNW80) were omitted from the study to reduce the number of animals sacrificed given that their TMAEA-co-NVP polymer composition is expected to be similar to the equivalent formulations without water. Histopathological examination of H&E stained stomach, intestine, colon, heart, liver, kidney, and spleen tissues revealed that the printlets did not
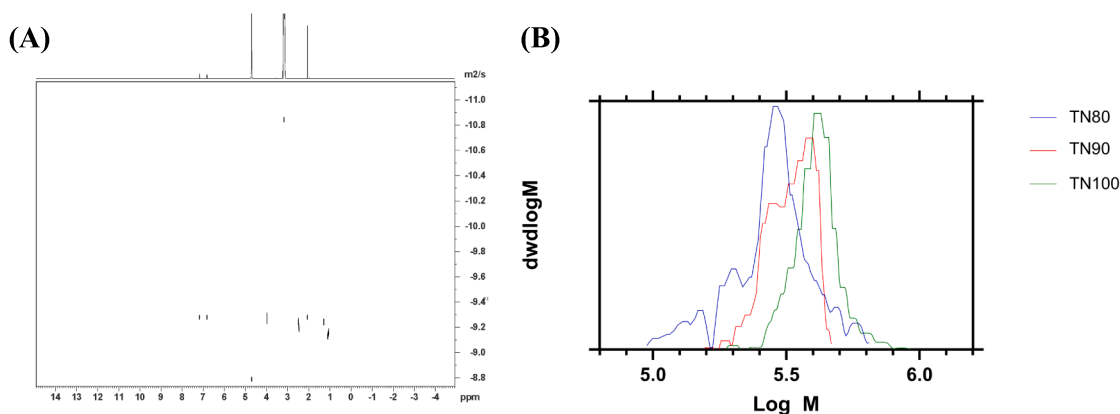
Fig. 8. (A) Exemplar ^{1}H DOSY NMR spectra of TN80 showing diffusion coefficient (D, y-axis) *vs.* [1]H chemical shift (∂, x-axis). Resonances are clearly visible for the paracetamol (7.2, 6.7 and 3.6 ppm ∂) at D ≈ 5.0 x 10^{-10} m^2/s with the resonances for the polymer (3.1 ppm ∂) at D ≈ 1.0 x 10^{-11} m^2/s, though slight differences between the samples are observed (see ESI). Residual water in the system is present as a singlet (4.7 ppm ∂) with D = 1.5 x 10^{-9} m^2/s which indicates variations within in-solution viscosity. (B) Apparent molar mass distributions of TN80, TN90 and TN100 extracted from diffusion within the side chain methyl peak (3.1 ppm ∂) to provide indicative polymer number average molar mass weighted by [H] signal intensity.
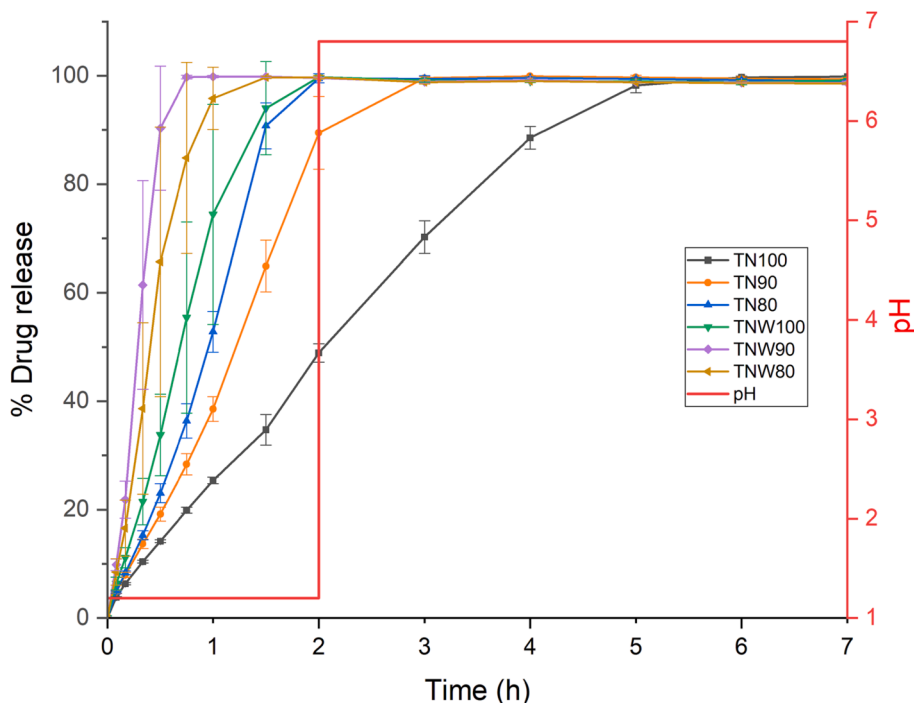
Fig. 9. Drug release profiles for TN100, TN90, TN80, TNW100, TNW90, and TNW80 printlets. The pH values of the dissolution media are indicated with the red line.

cause any significant tissue damage (Fig. 10). In addition, there were no significant changes in body weight over time for animals receiving the TN100, TN90, and TN80 printlets (Supplementary Table S2). No behavioural abnormality (e.g., changes to food consumption) was observed in any rats that received the printlets after administration until

the point of sacrifice. Collectively, these results suggest that single-dose administration of TN100, TN90, and TN80 printlets did not cause harm to the rats. Future studies to investigate the toxicity of the printlets upon repeated administration, given these printlets are likely to be consumed once or twice daily, will need to be performed to ascertain the safety of
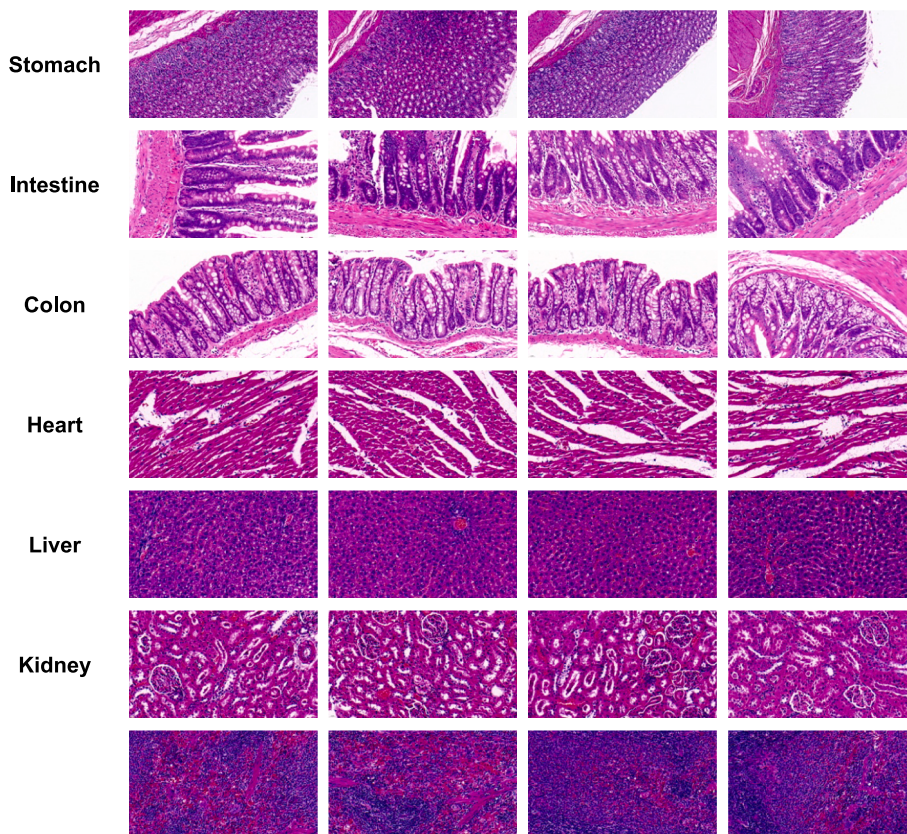

Fig. 10. Representative images of H&E stained stomach, intestine, colon, heart, liver, kidney, and spleen tissues harvested at 14 days post-administration.

the printlets.

The resins used in vat photopolymerization 3DP for medical purposes, such as SLA and DLP, have thus far consist of multi-functionalised (meth)acrylate monomers as the primary photopolymer and cross-linking agent. Consequently, the dense crosslinked matrix formed by these resins under light irradiation are insoluble in gastrointestinal fluids. In turn, the drug release profiles of the resulting dosage forms and medical devices follow sustained release kinetics, typically taking hours to days for the entire drug load to be released. This may be clinically undesirable especially given the historically low drug load (5–10%) of these delivery vehicles. The data presented above demonstrates the successful fabrication of drug-loaded, water-soluble printlets using DLP 3DP. Preliminary *in vivo* single-dose acute toxicity studies suggest that these formulations may not cause harm to animals. Consequently, medicinal oral dosage forms with a greater range of drug release profiles may now be fabricated with vat photopolymerization-based 3DP.

4. Conclusion

Water-soluble drug-loaded printlets were successfully printed, for the first time, using DLP 3DP. The loaded paracetamol was completely released from the printlets between 45 mins to 5 h, wherein the presence of water and NVP accelerated the drug release rate. The occurrence of phase separation during vat photopolymerization 3DP could have led to the paracetamol loading in printlets containing water being marginally lower than the theoretical paracetamol load. NMR spectroscopy analysis revealed that only trace amount of TMAEA and NVP monomers remained in the printlets after post-curing, and DOSY NMR measurements found that the polymerised polymers had a large apparent size exceeding 300,000 Da. Findings from *in vivo* single-dose acute toxicity studies in rats suggest that the printlets do not cause any tissue damage. By using water-soluble supramolecular polymer networks as opposed to insoluble cross-linked polymer networks, the versatility of drug release profiles that may be obtained with vat photopolymerization and consequently its application in the pharmaceutical space may be expanded. With further optimization, the high dimensional accuracy of vat photopolymerization may be harnessed for the fabrication of personalised medicines with complex and intricate geometries.

CRediT authorship contribution statement

Jun Jie Ong: Conceptualization, Data curation, Formal analysis, Investigation, Methodology, Visualization, Writing – original draft, Writing – review & editing. **Georgina Chow:** Data curation, Formal analysis. **Simon Gaisford:** Supervision, Formal analysis, Writing – review & editing. **Michael T. Cook:** Formal analysis, Writing – review & editing. **Thomas Swift:** Data curation, Formal analysis, Investigation, Writing – review & editing. **Richard Telford:** Data curation, Formal analysis, Investigation, Writing – review & editing. **Stephen Rimmer:** Data curation, Investigation. **Yujia Qin:** Data curation, Formal analysis, Investigation. **Yang Mai:** Methodology, Supervision, Resources. **Alvaro Goyanes:** Supervision, Writing – review & editing. **Abdul W. Basit:** Supervision, Resources, Writing – review & editing.

Declaration of Competing Interest

The authors declare the following financial interests/personal relationships which may be considered as potential competing interests: Alvaro Goyanes reports a relationship with FabRx that includes: equity or stocks. Abdul Basit reports a relationship with FabRx that includes: equity or stocks. A.W.B. Co-author is an editor for International Journal of Pharmaceutics.

Data availability

Data will be made available on request.

Appendix A. Supplementary data

Supplementary data to this article can be found online at https://doi.org/10.1016/j.ijpharm.2023.123286.

References

Adhami, M., Martin, N.K., Maguire, C., Courtenay, A.J., Donnelly, R.F., Domínguez-Robles, J., Larrañeta, E., 2023. Drug loaded implantable devices to treat cardiovascular disease. Expert Opin. Drug Deliv. 20, 507–522.

Alqahtani, M.S., Kazi, M., Alsenaidy, M.A., Ahmad, M.Z., 2021. Advances in oral drug delivery. Front. Pharmacol. 12.

American Society for Testing and Material, 2021. ISO/ASTM52900 Additive Manufacturing - General Principles - Fundamentals and vocabulary. ASTM.

Bagde, A., Dev, S., Madhavi K. Sriram, L., Spencer, S.D., Kalvala, A., Nathani, A., Salau, O., Mosley-Kellum, K., Dalvaigari, H., Rajaraman, S., Kundu, A., Singh, M., 2023. Biphasic burst and sustained transdermal delivery in vivo using an AI-optimized 3D-printed MN patch. Int. J. Pharm. 636, 122647.

Cui, S., Wang, Y., Gong, Y., Lin, X., Zhao, Y., Zhi, D., Zhou, Q., Zhang, S., 2018. Correlation of the cytotoxic effects of cationic lipids with their headgroups. Toxicol. Res. 7, 473–479.

Dawood, A., Marti, B.M., Sauret-Jackson, V., Darwood, A., 2015. 3D printing in dentistry. Br. Dent. J. 219, 521–529.

de Beer Martin, P., van der Laan Harry, L., Cole Megan, A., Whelan Riley, J., Burns Mark, A., Scott Timothy, F., 2019. Rapid, continuous additive manufacturing by volumetric polymerization inhibition patterning. Sci. Adv. 5, eaau8723.

de Oliveira, R.S., Fantaus, S.S., Guillot, A.J., Melero, A., Beck, R.C.R., 2021. 3D-printed products for topical skin applications: from personalized dressings to drug delivery. Pharmaceutics 13, 1946.

de Oliveira, R.S., Funk, N.L., dos Santos, J., de Oliveira, T.V., de Oliveira, E.G., Petzhold, C.L., Costa, T.M.H., Benvenutti, E.V., Deon, M., Beck, R.C.R., 2023. Bioadhesive 3D-printed skin drug delivery polymeric films: from the drug loading in mesoporous silica to the manufacturing process. Pharmaceutics 15, 20.

Deon, M., dos Santos, J., de Andrade, D.F., Beck, R.C.R., 2022. A critical review of traditional and advanced characterisation tools to drive formulators towards the rational development of 3D printed oral dosage forms. Int. J. Pharm. 628, 122293.

Deore, B., Sampson, K.L., Lacelle, T., Kredentser, N., Lefebvre, J., Young, L.S., Hyland, J., Amaya, R.E., Tanha, J., Malenfant, P.R.L., de Haan, H.W., Paquet, C., 2021. Direct printing of functional 3D objects using polymerization-induced phase separation. Nat. Commun. 12, 55.

Detamornrat, U., McAlister, E., Hutton, A.R.J., Larrañeta, E., Donnelly, R.F., 2022. The role of 3D printing technology in microengineering of microneedles. Small 18, 2106392.

Economidou, S.N., Pere, C.P.P., Reid, A., Uddin, M.J., Windmill, J.F.C., Lamprou, D.A., Douroumis, D., 2019. 3D printed microneedle patches using stereolithography (SLA) for intradermal insulin delivery. Mater. Sci. Eng. C 102, 743–755.

Elbadawi, M., McCoubrey, L.E., Gavins, F.K.H., Ong, J.J., Goyanes, A., Gaisford, S., Basit, A.W., 2021. Harnessing artificial intelligence for the next generation of 3D printed medicines. Adv. Drug Deliv. Rev. 175, 113805.

Gittard, S.D., Ovsianikov, A., Akar, H., Chichkov, B., Monteiro-Riviere, N.A., Stafslien, S., Chisholm, B., Shin, C.-C., Shih, C.-M., Lin, S.-J., Su, Y.-Y., Narayan, R.J., 2010. Two photon polymerization-micromolding of polyethylene glycol-gentamicin sulfate microneedles. Adv. Eng. Mater. 12, B77–B82.

Han, D., Morde, R.S., Mariani, S., La Mattina, A.A., Vignali, E., Yang, C., Barillaro, G., Lee, H., 2020. 4D printing of a bioinspired microneedle array with backward-facing barbs for enhanced tissue adhesion. Adv. Funct. Mater. 30, 1909197.

Janusziewicz, R., Mecham, S.J., Olson, K.R., Benhabbour, S.R., 2020. Design and characterization of a novel series of geometrically complex intravaginal rings with digital light synthesis. Adv. Mater. Technol. 5, 2000261.

Jørgensen, A.K., Ong, J.J., Parhizkar, M., Goyanes, A., Basit, A.W., 2023. Advancing non-destructive analysis of 3D printed medicines. Trends Pharmacol. Sci. 44, 379–393.

Kelly, B.E., Bhattacharya, I., Heidari, H., Shusteff, M., Spadaccini, C.M., Taylor, H.K., 2019. Volumetric additive manufacturing via tomographic reconstruction. Science 363, 1075–1079.

Li, W., Mille, L.S., Robledo, J.A., Uribe, T., Huerta, V., Zhang, Y.S., 2020. Recent advances in formulating and processing biomaterial inks for vat polymerization-based 3D printing. Adv. Healthc. Mater. 9, 2000156.

Lim, S.H., Kathuria, H., Amir, M.H.B., Zhang, X., Duong, H.T.T., Ho, P.-C.-L., Kang, L., 2021. High resolution photopolymer for 3D printing of personalised microneedle for transdermal delivery of anti-wrinkle small peptide. J. Control. Release 329, 907–918.

Loterie, D., Delrot, P., Moser, C., 2020. High-resolution tomographic volumetric additive manufacturing. Nat. Commun. 11, 1–6.

Martin, N.K., Domínguez-Robles, J., Stewart, S.A., Cornelius, V.A., Anjani, Q.K., Utomo, E., García-Romero, I., Donnelly, R.F., Margariti, A., Lamprou, D.A., Larrañeta, E., 2021. Fused deposition modelling for the development of drug loaded cardiovascular prosthesis. Int. J. Pharm. 595, 120243.

Medicines & Healthcare products Regulatory Agency, 2021. Consultation on Point of Care manufacturing, gov.uk.

Ng, W.L., Lee, J.M., Zhou, M., Chen, Y.-W., Lee, K.-X.-A., Yeong, W.Y., Shen, Y.-F., 2020. Vat polymerization-based bioprinting—process, materials, applications and regulatory challenges. Biofabrication 12, 022001.

Paquet, C., Deore, B., de Haan, H., Orth, A., Lacelle, T., Zhang, Y., Sampson, K., 2022. Diffusion and phase separation in vat polymerization 3D printing. SPIE.

Pereira, B.C., Isreb, A., Isreb, M., Forbes, R.T., Oga, E.F., Alhnan, M.A., 2020. Additive manufacturing of a Point-of-Care "Polypill:" Fabrication of concept capsules of complex geometry with bespoke release against cardiovascular disease. Adv. Healthc. Mater. 9, 2000236.

Ranganathan, S.I., Kohama, C., Mercurio, T., Salvatore, A., Benmassaoud, M.M., Kim, T. W.B., 2020. Effect of temperature and ultraviolet light on the bacterial kill effectiveness of antibiotic-infused 3D printed implants. Biomed. Microdevices 22, 59.

Robles-Martinez, P., Xu, X., Trenfield, S.J., Awad, A., Goyanes, A., Telford, R., Basit, A. W., Gaisford, S., 2019. 3D printing of a multi-layered polypill containing six drugs using a novel stereolithographic method. Pharmaceutics 11, 274.

Rodríguez-Pombo, L., Xu, X., Seijo-Rabina, A., Ong, J.J., Alvarez-Lorenzo, C., Rial, C., Nieto, D., Gaisford, S., Basit, A.W., Goyanes, A., 2022. Volumetric 3D printing for rapid production of medicines. Addit. Manuf. 52, 102673.

Rodríguez-Pombo, L., Martínez-Castro, L., Xu, X., Ong, J.J., Rial, C., García, D.N., González-Santos, A., Flores-González, J., Alvarez-Lorenzo, C., Basit, A.W., Goyanes, A., 2023. Simultaneous fabrication of multiple tablets within seconds using tomographic volumetric 3D printing. Int. J. Pharm.: X 5, 100166.

Rouzé l'Alzit, F., Cade, R., Naveau, A., Babilotte, J., Meglioli, M., Catros, S., 2022. Accuracy of commercial 3D printers for the fabrication of surgical guides in dental implantology. J. Dentistry 117, 103909.

Seoane-Viaño, I., Xu, X., Ong, J.J., Teyeb, A., Gaisford, S., Campos-Álvarez, A., Stulz, A., Marcuta, C., Kraschew, L., Mohr, W., Basit, A.W., Goyanes, A., 2023. A case study on decentralized manufacturing of 3D printed medicines. Int. J. Pharm.: X 5, 100184.

Swift, T., Hoskins, R., Telford, R., Plenderleith, R., Pownall, D., Rimmer, S., 2017. Analysis using size exclusion chromatography of poly(N-isopropyl acrylamide) using methanol as an eluent. J. Chromatogr. A 1508, 16–23.

Tiboni, M., Campana, R., Frangipani, E., Casettari, L., 2021. 3D printed clotrimazole intravaginal ring for the treatment of recurrent vaginal candidiasis. Int. J. Pharm. 596, 120290.

Trivedi, M.K., Patil, S., Shettigar, H., Bairwa, K., Jana, S., 2015. Effect of biofield treatment on spectral properties of paracetamol and piroxicam. Chem. Sci. J. 6.

Utomo, E., Domínguez-Robles, J., Anjani, Q.K., Picco, C.J., Korelidou, A., Magee, E., Donnelly, R.F., Larrañeta, E., 2023. Development of 3D-printed vaginal devices containing metronidazole for alternative bacterial vaginosis treatment. Int. J. Pharm.: X 5, 100142.

van Lith, R., Baker, E., Ware, H., Yang, J., Farsheed, A.C., Sun, C., Ameer, G., 2016. 3D-printing strong high-resolution antioxidant bioresorbable vascular stents. Adv. Mater. Technol. 1, 1600138.

Vehse, M., Petersen, S., Sternberg, K., Schmitz, K.-P., Seitz, H., 2014. Drug delivery from poly(ethylene glycol) diacrylate scaffolds produced by DLC based micro-stereolithography. Macromol. Symp. 346, 43–47.

Vivero-Lopez, M., Xu, X., Muras, A., Otero, A., Concheiro, A., Gaisford, S., Basit, A.W., Alvarez-Lorenzo, C., Goyanes, A., 2021. Anti-biofilm multi drug-loaded 3D printed hearing aids. Mater. Sci. Eng. C 119, 111606.

Wilts, E.M., Pekkanen, A.M., White, B.T., Meenakshisundaram, V., Aduba, D.C., Williams, C.B., Long, T.E., 2019. Vat photopolymerization of charged monomers: 3D printing with supramolecular interactions. Polym. Chem. 10, 1442–1451.

Xu, X., Robles-Martinez, P., Madla, C.M., Joubert, F., Goyanes, A., Basit, A.W., Gaisford, S., 2020. Stereolithography (SLA) 3D printing of an antihypertensive polyprintlet: Case study of an unexpected photopolymer-drug reaction. Addit. Manuf. 33, 101071.

Xu, X., Awad, A., Robles-Martinez, P., Gaisford, S., Goyanes, A., Basit, A.W., 2021a. Vat photopolymerization 3D printing for advanced drug delivery and medical device applications. J. Control. Release 329, 743–757.

Xu, X., Goyanes, A., Trenfield, S.J., Diaz-Gomez, L., Alvarez-Lorenzo, C., Gaisford, S., Basit, A.W., 2021b. Stereolithography (SLA) 3D printing of a bladder device for intravesical drug delivery. Mater. Sci. Eng. C 120, 111773.

Xu, X., Seijo-Rabina, A., Awad, A., Rial, C., Gaisford, S., Basit, A.W., Goyanes, A., 2021c. Smartphone-enabled 3D printing of medicines. Int. J. Pharm. 609, 121199.

Yang, Y., Zhou, Y., Lin, X., Yang, Q., Yang, G., 2020. Printability of external and internal structures based on digital light processing 3D printing technique. Pharmaceutics 12.

Yao, W., Li, D., Zhao, Y., Zhan, Z., Jin, G., Liang, H., Yang, R., 2020. 3D printed multi-functional hydrogel microneedles based on high-precision digital light processing. Micromachines 11, 17.